Supporting information for

Morphology of soft and rough contact via fluid drainage

Yumo Wang[1,3] and Joelle Frechette[1,2]

[1]Chemical and Biomolecular Engineering Department and [2]Hopkins Extreme Materials Institute, Johns Hopkins University, Baltimore MD 21218 USA. \

[3]National Engineering Laboratory for Pipeline Safety, Beijing Key Laboratory of Urban Oil and Gas Distribution Technology, China University of Petroleum, Beijing, 18# Fuxue Road, Changping District, 102249 Beijing, China

1. Summary of experimental parameters

Type	Physical parameter	Sample 1	Sample 2	Sample 3	Sample 4
PDMS film	Thickness, T	330 μm	147μm	54 μm	11 μm
	Disk 1: R_1	1.62 cm	1.32 cm	1.64 cm	1.18 cm
	Disk 2: R_2	1.89 cm	1.86 cm	2.28 cm	1.02 cm
	$R_h = 2R_1R_2/(R_1+R_2)$	1.74 cm	1.53 cm	1.91 cm	1.09 cm
	$R_g = R = (R_1R_2)^{1/2}$	1.75 cm	1.55 cm	1.91 cm	1.10 cm
	Young's modulus, E	0.95 MPa	1.05 MPa	1.05 MPa	0.95 MPa
	Poisson's ratio, v	0.5			
SFA	Spring constant, k	165.3 N/m			
	Drive velocity, V	50-150 nm/s			
	Initial separation, $h(0,0)$	2-5 μm			
	Maximum motor travel	10 μm			
	SU-8 thickness	6-7 um			
	Mica thickness	3-10 um			
	Top silver thickness	50 nm			
Fluid (silicone oil)	Viscosity, η_{fluid}	0.2 Pa·s			
	Density, ρ	0.98 g/cm^3			

Table S1: Overview of the experimental parameters investigated.

Our experiments are performed between crossed-cylinders (equivalent to the sphere-plane geometry when R >> h) using the Surface Forces Apparatus (SFA). One surface is rigid (bottom in Fig. S1) and the other is compliant due to the presence of a PDMS film (polydimethylsiloxane) coated with a 50 nm silver film as a top layer and deposited, silver side up, on a mica sheet (Fig. S1). The silver layer serves a mirror for the interferometer and prevents swelling of the PDMS with the silicone oil fluid.

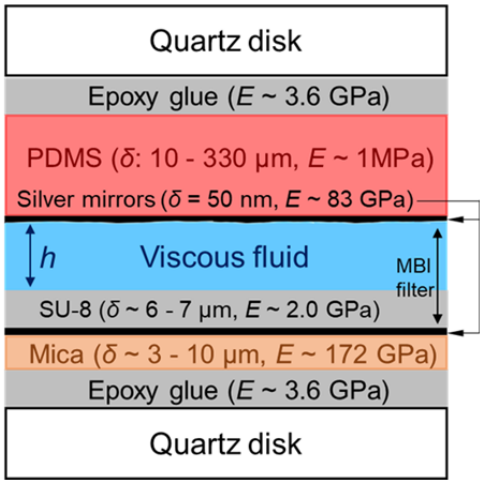

Figure S1: Top and bottom surfaces in SFA with detailed material layers and properties.

2. Surface characterization

2.1. Determination of Young's modulus of the bulk PDMS

We determine independently the Young's modulus of polydimethyl siloxane (PDMS) via indentation measurements with a spherical probe. We use a homemade Multimode Force Microscope[1] and compare the force-indentation results with layered indentation theory. The contact area is measured by a high-speed CMOS camera (FLIR GS3-U3-23S6C-C) and fitted to circular shape using ImageJ to determine contact radius. Meanwhile, the normal applied force is measured by a cantilever spring (k=1055N/m), and the radius of the indentor is 3.175 mm, which is greater than the coating thickness.

To obtain the Young's modulus of PDMS we need to account for the effect of stratification on the indentation measurements. We follow the analytical corrections presented by Shull[2], applying corrections factors on indentation depth (σ), normal force (F) and contact radius (a) to a Hertzian contact model. The correction factors used are listed follows:

$$f_p(a/\delta) = (1+\beta(a/\delta)^3) \tag{S1}$$

$$f_\sigma(a/\delta) = \left(0.4 + 0.6\exp\left(\frac{-1.8a}{\delta}\right)\right) \tag{S2}$$

$$\frac{1}{f_c(a/\delta)} = 1 + \left(\frac{0.75}{(a/\delta)+(a/\delta)^3} + \frac{2.8(1-2\nu)}{a/\delta}\right)^{-1}, \tag{S3}$$

and the Hertzian contact model changes to:

$$\sigma = \frac{a^2}{R} f_\sigma(a/\delta) + \frac{f_c(a/\delta)}{2E^*\delta}\left(F - \frac{4E^*a^3}{3R} f_p(a/\delta)\right), \tag{S4}$$

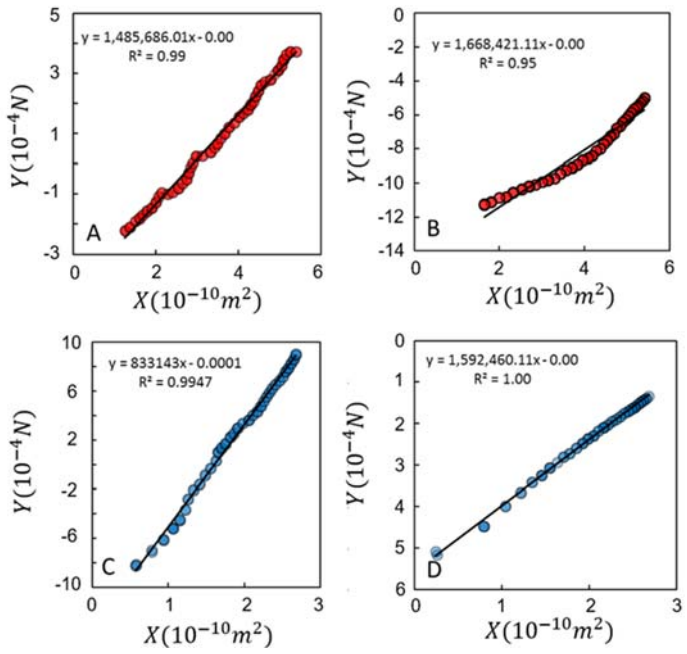

Figure S2: Experimental data of and linear fit of Y vs. X for various PDMS thicknesses and motion mode. (A) and (B): PDMS coating of 147μm. (C) and (D): PDMS coating of 54μm. (A) and (C): spherical indenter of radius 3.175mm approaching tested sample. (B) and (D): indenter retracting from sample.

which can be rearranged to:

$$\left(\left(\delta-\frac{a^2}{R}f_\sigma(a/h)\right)2a+f_c(a/h)\frac{4a^3}{3R}f_p(a/h)\right)E^*=f_c(a/h)F\ , \qquad \text{(S5)}$$

or in simplified notations:

$$XE^*=Y\ . \qquad \text{(S6)}$$

The experimental data are then compared with the linear relationship between Y and X to extract E^* as the slope. The results are shown in Figure S2 for PDMS films with two thicknesses (147μm, A and B; 54μm, C and D), for both approach (A and C) and retraction (B and D). The plots show good general linearity in Y vs. X, which verifies the suitability of the corrections used. The average measured reduced Young's modulus of PDMS is then calculated as 1.39MPa and Young's modulus $E=E^*(1-\nu^2)$ as $1.05\pm0.15MPa$ with Poisson's ratio set to be 0.5. We also performed indentation experiments directly in the SFA in our previous work[3], where we treated a 330μm thick film as an approximated half-space and we applied semi-infinite JKR theory to get a modulus of $1.08\pm0.05MPa$, including the rigid substrate contributions. If we re-fit same data with layered equations mentioned above, the absolute modulus without the substrate effects obtained is $0.95\pm0.05MPa$. The difference between the two measurements is therefore about 9.1%. To compare our results with different thicknesses, we apply here the 0.95MPa modulus to the 330μm film.

2.2. Characterization of the silvered-PDMS surfaces

Plasma-treatment of PDMS leads to a surface roughness on the order of 10*nm* [4]. In addition, subsequent thermal evaporation of silver on PDMS can further increase the surface roughness through the formation of small cracks of the oxidized surface layer, although large scale buckling is generally prevented [5]. We characterized the roughness of the surfaces employed in the SFA using an atomic force microscope, AFM (Dimension 3100, Bruker Nano, CA). We characterized the roughness (peak-to-valley difference) on silver-coated PDMS films with PDMS thickness of $\delta = 54\,\mu m$ and $\delta = 147\,\mu m$ and a silver thickness of 50 *nm*. Imaging was performed in the contact mode, on an area of $3 \times 3\,\mu m^2$ at a scan rate of 1.50*Hz* (Figure S3A, B). We found that within a sample (PDMS thickness) the root-mean square (RMS) roughness and peak-to-valley difference was fairly constant but that it varied from sample to sample. The $\delta = 54\,\mu m$ sample has an average (RMS) roughness of 3.33*nm*, and a peak-to-valley difference of 22.00*nm*, while $\delta = 147\,\mu m$ film has a RMS roughness of 5.8 *nm* and a peak-to-valley difference of 49.9*nm*.

Poor wetting may generate surface slip and nano-bubbles during drainage. We measured the contact angle of silicone oil on top of silvered-PDMS surface, as shown in Figure S3C, and the average contact angle is 16.5 degrees. As expected, and verified here, the silicone oil wets the silvered-PDMS.

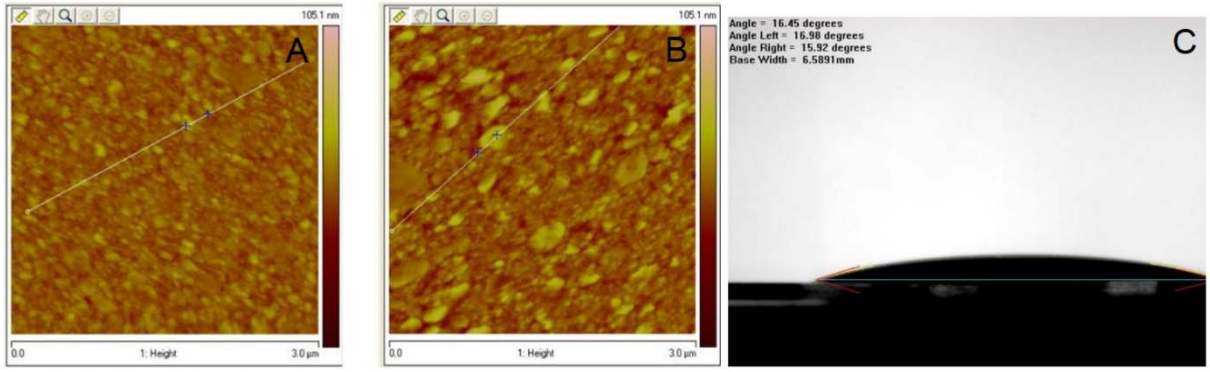

Figure S3: AFM images of silver coated PDMS films where the PDMS thickness is $\delta = 54\,\mu m$ (A) and $\delta = 147\,\mu m$ (B). The height range is 105*nm* as shown in color bars on the side. (C) Contact angle of silicone oil on top of silvered-PDMS surface.

2.3. Predictions on surface morphology with different thickness and roughness

The apparent slip and elasticity have opposing but qualitatively different role on the drainage process. The morphology of the surface is almost uniquely determined by the mechanical properties of surfaces (coating thickness and elasticity), while the fluid gap shifts due to the apparent slip caused by roughness. To support this statement we show here in Figure S4 how varying the apparent slip length will change the fluid film thickness but not the deformation profile, as observed in our experiments.

The surface morphology using single shifted-plane value of 35*nm* is showed by blue solid line in Figure S4. The experimental data agree mostly with the prediction with a slight underestimation. Overall, the shape of the predicted curve recovers very well the wimple shape as observed during experiment. The shifted length (representing level of roughness) is varied in dotted and dot-dashed blue lines, with a value of 15 and 45*nm* used, respectively. We see that for both additional shifted lengths, the wimple shape is mostly recovered on these two curves, indicating that the surface morphology is mostly determined by mechanical properties, while the absolute surface position is highly influenced by surface roughness during drainage.

This effect is further demonstrated by the green solid line and black dotted line, in which incorrect coating thicknesses are used (changing the coating thickness leads to a larger effective modulus). For the green solid line, an underestimated thickness is used (δ = 30μm) while a no-slip boundary condition is incorporated to best fit the central position. We can see that: the morphology predicted in this case is clearly off, especially in the central region. Similarly, if we overestimate the coating thickness (half-space, black dotted line) and try to best fit the surface profile by using a large shifted length of 110nm, the morphology also doesn't match the experimental results, especially for the radial position > 100μm. These analyses prove that although both surface stratification and roughness facilitate drainage, their role played are qualitatively different, and in fact distinguishable from (and only from) the surface morphology. In the SFA experiments, the coating thickness and material Young's modulus are independently measured, therefore, the morphology of the soft coating is predicted without fitting parameter, and the shifted length is the only fitting parameter to predict the absolute separation. Thus, the role played by mechanical properties and surface roughness are decoupled.

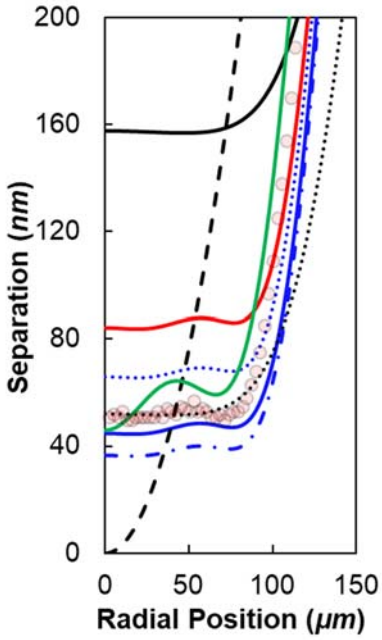

Figure S4: Predictions for the role of shifted length, PDMS coating thickness on fluid film profile. Coating thickness $\delta = 54\mu m$ **,** at t = 71.2s in Fig.4b. Data points are the experimental results. Predictions for stratified material with (red) no-slip and (blue) combined with a shifted plane correction of 35nm (blue solid), 15 nm (blue dotted) and 45nm (dot-dashed). Other lines are for half-space (black solid), rigid surfaces (black dashed). The green solid line underestimates the PDMS coating thickness (Green, δ = 30μm, no slip), and black dotted line overestimates the coating thickness. (Black dotted, half-space, shifted length = 110nm).

2.4. Effects of the thin silver layer (50 nm) on top of the soft layer

We do not expect the 50nm silver film on the PDMS to have significant constraint on the deformation of PDMS layer, because of the thickness of the silver film compared to that of the PDMS (50nm vs 10-330 microns) along with the large radius of curvature and hydrodynamic radius in the SFA(1-2cm). In addition,

the silver film has the added advantage of preventing swelling of the PDMS in the oil by blocking transport of the oil into the PDMS. It is possible that the top silver layer constrains the deformation of the PDMS layer, and could have an effect on the Young's modulus. Therefore, to estimate the role played by the silver film, a quick and convenient method to verify its contribution to an effective modulus is to use the numerical results for indentation of stratified films provided in Figures 2 & 3 of Ref. [6]. The Young's modulus of silver layer is at least 1000 times larger than the PDMS base (even for thin PDMS coating in our experiments, in which $\delta = 10.9\ \mu m$, the effective modulus in this case is ~ $80MPa$, as verified by indentation experiment), and the hydrodynamic radius much greater than the silver film thickness, the increase in Young's modulus result from the silver coating should be very small.

A more quantitative method to estimate the stiffening effects due to silver coating is to use the approximation of Eqn. 11 in Ref. [7]:

$$F_f = \pi E_f^* Y \left[\frac{-6a^6 + 6a^4 (R^+)^2 + Y^2 a^4 - 4Y^2 a^2 (R^+)^2}{6((R^+)^2 - a^2)^{5/2}} \right]. \qquad \text{(S7)}$$

In which, F_f is the effective extra load due to metal layer, E_f^* is the effective modulus of the metal film, R^+ is the curvature of the deformation during indentation. Y is the thickness of the metal film on top. We can further compare the modulus of the PDMS-Silver layers with and without the silver to get:

$$\frac{E_{sys(l)}^*}{E_{sys}^*} = 1 + \frac{3R\pi Y}{4a^3} \left[\frac{-6a^6 + 6a^4 (R^+)^2 + Y^2 a^4 - 4Y^2 a^2 (R^+)^2}{6((R^+)^2 - a^2)^{5/2}} \right]. \qquad \text{(S8)}$$

Based on Eqn. S8, we estimate the actual importance of silver layer on the apparent Young's modulus. The results show that the influence of the silver layer increases with the contacting area. At the largest possible hydrodynamic radius in our experiment (~$100s$ of μm), the stiffening due to the silver film is only about 0.5%, we can safely neglect the effect of the silver layer in our application.

3. SFA data processing and analysis

3.1. Multiple beam interferometry (MBI)

the SFA is designed to measure the forces acting between two surfaces as a function of their separation. The force is measured via the deflection of a cantilever on which the lower surfaces is mounted, and the surface separation is deduced independently using multiple beam interferometry (MBI)[8]. MBI relies on the construction of an interference filter, which consists of two reflective surfaces (here silver) separated by a dielectric medium. When white light is passed through such a filter, only certain wavelengths will emerge; all the other wavelengths interfere destructively and are not transmitted. The emerging wavelengths result in observable fringes (fringes of equal chromatic order, FECO). Optical theory relates the transmitted wavelength to an absolute surface separation with a resolution of 1-3 $\mathring{A}$. The resolution in normalized force is $1\mu N/m$. The separation between the surfaces is varied by using two microstepping motors moving the upper and lower micrometer rods. Two 50 nm-thick silver films, being highly reflective (>95%), yield sharp and high-contrast primary FECO. We use a CCD camera: Q-Imaging Retiga 4000RV, to capture the digital image of such FECO images after they are dispersed in an imaging spectrograph. Some examples of original FECO images that's appear on the spectrograph is shown below in Figure S5. Some of the snapshot of FECO images are colorized using ImageJ and shown directly in Figure 2 and Figure 6 to reveal contacting shape. For acquiring quantitative absolute separation, further analysis is needed as we present in next paragraph.

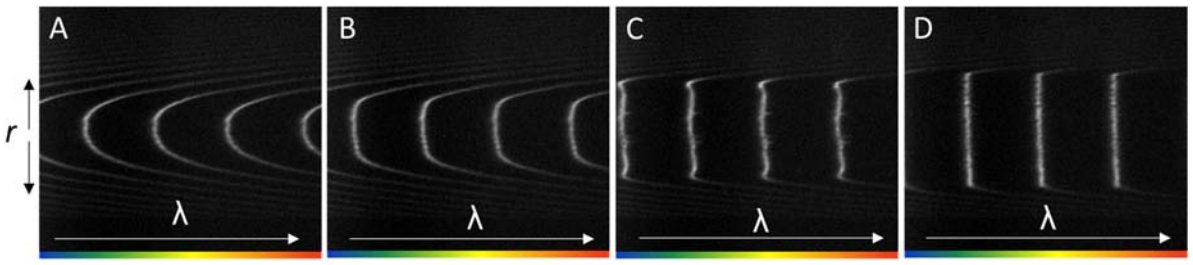

Figure S5: Examples of original FECO images acquired from spectrograph. A-D: images used in Figure 2A, panel II, from blue to yellow. White arrow indicate wavelength increasing direction, and black arrow indicate lateral position (r)

3.2. Data analysis

The center of mass (CoM) of the measured intensity as a function of pixel position is used to estimate pixel position for each of the peaks in the intensity. We use the pixel positions of the known discrete spectral wavelengths (green: 546nm and orange-yellow doublet: 577-579nm) of mercury to convert pixels into wavelengths of the FECO. Upon gluing to the cylindrical lens, the interference filter acquires curvature and the medium thickness and consequently, the wavelengths of the FECO are a function of lateral position. The presence of macroscopic surfaces enables the visualization of the 2-dimensional geometry of the interacting surfaces, which is reflected in the shape of the FECO.

The FECO obtained for two crossed-cylinders are used to calculate the radii of curvature of the interacting cylinders (Section 1). The wavelengths at the vertex of the parabolic fringes are used to estimate the surface separation at the point of closet approach (PCA) for a sphere-plane configuration. Estimation of radii of curvature and diameter of zone of contact requires the lateral resolution (typically $\approx 2.64\mu m$ as dictated by the optical magnification). The use of highly reflective silver suppresses the secondary, tertiary, and gap fringes. Note here that we use the center of mass of the interferometric fringes to determine their wavelengths and calculate the fluid film thickness. The FECO represent the summation of all intensity profiles corresponding to the point of lights transmitted through silver mirrors [9]. As a result, the fluid film thickness we measured is based on the center of mass of the asperities within each pixel (~2μm).

We employ the fast spectral correlation (FSC) algorithm devised by Heuberger to facilitate transformation or inversion of transmitted intensity to unknown medium thickness and/or index of refraction [10]. In FSC, the sum of transmitted intensity for multiple experimentally observed wavelengths for a range of medium thickness and/or index of refraction is examined, and the unknown parameter or combination of parameters that results in the maximum transmissivity is used as the solution. We use an in-house LabVIEW interface to facilitate dynamic measurements as well as automated analysis of FECO images. For more details regarding the image processing and analysis, the readers are directed to Ref. [11].

4. Definition of contact position (zero separation)

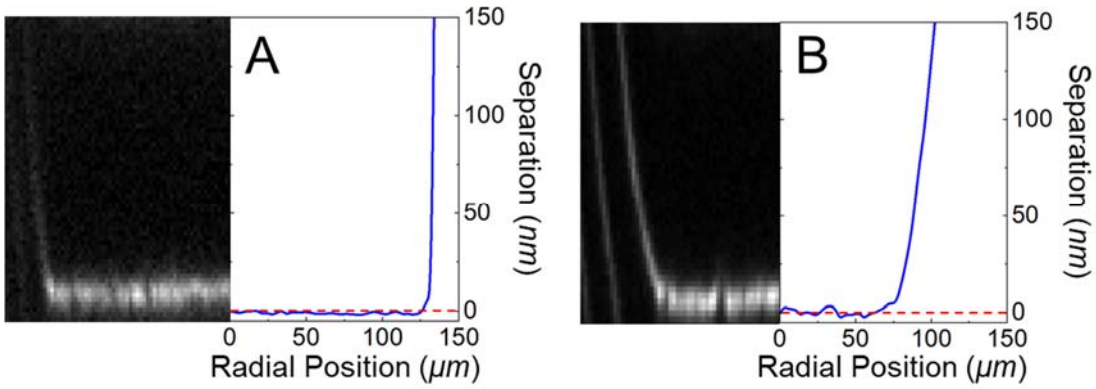

Figure S6: Examples of contact position captured in quasi-static SFA experiments, left side: pictures of an individual interferometric fringe. Right sides: analyzed separation data showing the lateral variation of contact shape. A: Experiment for $\delta = 54\mu m$, case II in Fig.2. B: Experiment for $\delta = 147\mu m$, case III in Fig.2. The dashed red lines indicate the defined zero separation position (contact) based on central pixels.

The contact position (zero separation) is defined through quasi-static experiments in which the surfaces were slowly pushed together until a large central contact regime is formed (Fig. S6). We mark the position at the center pixel (point of closest approach) and use it as the reference position for zero separation throughout (red dashed lines in Fig. S6). The lateral variation of this contact position is typically less than 0.5 *nm*, as shown in Fig.S6A for case II in Fig.2, and same level of smoothness applies to Case I and IV in Fig.2. The lateral variation of contact position in these cases can be attributed to the roughness of the silver layer. For some cases (case III in Fig. 2) the tilting or unevenness of underlying SU-8 can affect the contact morphology in which the maximum spacial variation can be 5 *nm*, as shown by Fig. S6B.

References

[1] P. Roberts, G.A. Pilkington, Y. Wang, J. Frechette, A multifunctional force microscope for soft matter with in situ imaging, Review of Scientific Instruments, 89 (2018) 043902.

[2] K.R. Shull, Contact mechanics and the adhesion of soft solids, *Materials Science and Engineering: R: Reports* 36 (2002) 1-45.

[3] Y. Wang, C. Dhong, J. Frechette, Out-of-contact elastohydrodynamic deformation due to lubrication forces, *Physical Review Letters*, 115 (2015) 248302.

[4] J. Bongaerts, K. Fourtouni, J. Stokes, Soft-tribology: lubrication in a compliant PDMS–PDMS contact, *Tribology International* 40 (2007) 1531-1542.

[5] J.P. Déry, D. Brousseau, M. Rochette, E.F. Borra, A.M. Ritcey, Aluminum-coated elastomer thin films for the fabrication of a ferrofluidic deformable mirror, *Journal of Applied Polymer Science*, 134 (2017) 44542.

[6] A. Perriota and E. Barthel, Elastic contact to a coated half-space: Effective elastic modulus and real penetration, *Journal of Materials Research,* 19.2 (2004): 600-608.

[7] F. K. Yang, W. Zhang, Y. G. Han, S. Yoffe, Y. C. Cho, and B. X. Zhao, "Contact" of Nanoscale Stiff Films, *Langmuir* 28, 9562 (2012).

[8] J. Israelachvili, Thin film studies using multiple-beam interferometry, *Journal of Colloid & Interface Science*, 44 (1973) 259-272.

[9] J.M. Levins, T.K. Vanderlick, Impact of roughness of reflective films on the application of multiple beam interferometry, *Journal of Colloid & Interface Science*, 158 (1993) 223-227.

[10] M. Heuberger, The extended surface forces apparatus. Part I. Fast spectral correlation interferometry, *Review of Scientific Instruments*, 72 (2001) 1700-1707.

[11] Y. Wang, Deformation of compliant coatings due to lubrication forces, Ph.D. thesis, Johns Hopkins University, 2017.